Solidification of a high-Reynolds-number flow in laser percussion drilling

W. R. Smith[†] and R. M. M. Mattheij[‡]
[†]School of Mathematics and Statistics, The University of Birmingham, Edgbaston, Birmingham, B15 2TT, UK
[‡]Department of Mathematics and Computing Science, Technische Universiteit Eindhoven, PO Box 513, 5600 MB Eindhoven, The Netherlands

Abstract

An extension to the enthalpy method is developed to study the solidification of a high-Reynolds-number flow moving across a solid surface. The competition between inertia, melting and freezing is investigated for the flow of molten aluminium across a cool solid aluminium surface. The molten aluminium initially freezes due to rapid thermal conduction into the solid. If the molten aluminium has sufficient sensible heat, the chill melts back and melting of the original solid follows. If the molten aluminium has insufficient sensible heat, solidification continues until the passing of the trailing edge of the liquid/gas interface or the flow is engulfed. The rate of solidification may be reduced by introducing a decreasing initial velocity profile, but this results in fluid clumping. The results are interpreted in terms of the recast and bellow shape observed during laser percussion drilling.

1 Introduction

Laser percussion drilling is used to machine gas turbine components which are typically made out of super-alloys; these materials cannot be machined with conventional mechanical drills. The term percussion refers to the repeated operation of the laser in short pulses (10^{-3}s) which are separated by longer time periods (10^{-2}s). The laser builds up energy at a bounded rate and operation in this manner allows for large bursts of energy. Percussion drilling is favoured over other processes, such as spark erosion drilling or laser trepanning drilling, because it is by far the quickest. However, it suffers from three drawbacks (i) recast of solidified material at the wall of the hole, (ii) bellow shape, that is the local increase of hole diameter and (iii) tapering, that is the decrease of hole diameter with depth. Experimental results have also shown that the penetration depth is limited.

In laser percussion drilling, the metal is ablated by a combination of evaporation and melt ejection. However, the mass fraction extracted by evaporation is typically less than a tenth of the total mass loss [1, p. 133]. The melt ejection can be split into three different stages, shown in Figure 1. Initially a thin region of molten metal is formed by the absorption of laser energy at the target surface. This thin molten region at the base of the hole is known as the melt pool. Eventually, the irradiated surface reaches the vaporization temperature. A splash occurs in which the molten metal is pushed radially by the pressure gradients generated by the sudden expansion of the vapour evaporating from the surface (see the photographs of the early stages of melt ejection [1, p. 133]). The high recoil pressures involved also cause significant variation in the vaporization temperature and rapid flow of the vapour and air away from the irradiated surface [7]. The molten metal now has a high velocity and it can escape from the hole. However, this liquefied material can resolidify before it escapes from the hole. The walls of the hole are relatively cold and large temperature gradients occur across the thin film. The solid metal left exposed after the splash now starts to absorb laser energy and so on. In this paper, we will be concerned with simulating the solidification of the thin film as it moves along the side wall of the hole.

A series of photographs of a hole machined by laser percussion drilling is shown in Figure 2. The number denotes the number of pulses used to create the hole. The growth rate of the hole is initially constant but slows in the later photographs. The eleventh hole appears to be not as deep as the tenth, because the melt pool has solidified at the base of the hole in such a way as to obscure the base. The melt pool has probably solidified at the base of the hole because the pulse ended before the splash had been completed. We note

that the seventh and subsequent photographs show the resolidified material on the wall of the hole. This resolidification may be in the form of very thin layers, or more irregular clumps. In the last three photographs molten metal will have escaped via the bottom exit. There may be variability in the laser characteristics, in particular the radial, azimuthal and temporal intensity profile; this makes repeatability of experimental results very difficult, even with an identical set-up.

In the absence of experimental data, it is not possible to say whether or not the superalloys under consideration melt and solidify over a range of temperatures. The laser percussion drilling of aluminium will be considered here; aluminium is known to have a single melting point. Therefore, mushy regions will not be considered.

The subject of laser percussion drilling has been studied by several authors (see [3] and references therein). The fluid is modelled by the incompressible Navier-Stokes equations including gravity. These equations are currently exclusively solved by numerical approaches, which require extensive computing resources [4]. In [7], it was noted that the aspect ratio in the melt pool was small. Perturbation methods were employed to simplify the incompressible Navier-Stokes equations taking advantage of this aspect ratio. We consider the leading-order solidification model derived in [7], in which only the most significant physical effects have been retained. This leading-order problem simplifies the system of equations for two reasons. (a) The equations for conservation of mass and momentum are no longer field equations to be solved between the interfaces. The equation for conservation of energy is the only field equation. (b) A differential equation describes the shape of the liquid/gas interface and only the solid/liquid interface remains as a bona fide moving boundary. A recent review of a wide range of moving boundary problems and solution techniques is given in [5].

The enthalpy method is used to simulate phase changes due to thermal conduction in a fixed domain (see, for example, [2, 5]). Laser percussion drilling involves the flow over a solid surface. There are two significant differences with the conventional technique. (A) The equation for conservation of energy includes convection terms. (B) The domain of computation expands as the flow traverses the solid. In this paper, we describe the implementation of an extension to the enthalpy method in order to deal with these points.

The purpose of this paper is to gain a better understanding of the process of laser percussion drilling. The eventual aim is to select parameters to minimize the three drawbacks associated with laser percussion drilling. The process depends on the material properties, ambient conditions and laser characteristics.

The contents of the paper will now be outlined. A mathematical model for the solidification of a high-Reynolds-number flow is introduced in Section 2. The governing equations are a combination of the shallow water equations in the zero gravity limit and a two-phase Stefan problem. Section 3 describes the implementation of the extension to the enthalpy method. Three simulations are undertaken in Section 4. The first and second simulations differ in the size of the initial blob and its temperature gradient. The first and third simulations are identical apart from the initial conditions for velocity. This third simulation corresponds to the development of a shock. Finally, Section 5 interprets the numerical results in terms of laser percussion drilling.

2 Mathematical Model

The different parameters in the model depend on laser set-up, the material to be drilled and the local temperature, which for aluminium may vary from 300K to approximately 2500K. For the drilling of aluminium the parameters are given in Table 1 (see, for example, [6]). With a length-scale of $L \sim 10^{-3}$m and thickness $d \sim 10^{-4}$m, a typical aspect ratio is given by $\delta = d/L \sim 0.1$. With a typical maximum velocity given by $U \sim 50\text{ms}^{-1}$ (see [1, p. 132]), the dimensionless parameters are

$$Re = \frac{\rho U L}{\mu} \sim 5 \times 10^4, \quad Fr = \frac{U^2}{Lg} \sim 3 \times 10^5, \quad Pe = \frac{\rho c U L}{k} \sim 5 \times 10^2,$$

$$Br = \frac{\mu U^2}{k(T_v - T_m)} \sim 2 \times 10^{-5}, \quad We = \frac{\rho U^2 L}{\sigma} \sim 7 \times 10^3,$$

where g is the acceleration due to gravity. The order of the parameters motivates us to consider inviscid flow with heat convection and conduction, neglecting viscous boundary layers, surface tension and gravity.

The three stages in the melt ejection described above and shown in Figure 1 are (i) melt-pool formation, (ii) a splash in which the melt pool is accelerated out of the base of the hole and (iii) the solidification process in which the hot fluid is moving across the cold side wall of the drilled hole. We will not discuss (i) and (ii). (iii) Once the fluid has moved away from the base of the hole, there is competition between inertia, melting and solidification as a fluid ring moves up the cold side wall of the drilled hole. The radius of curvature of the side wall is so much larger than the melt thickness, that we will work in a planar idealization for the solidification model as shown in Figure 3. The vertical direction is perpendicular to the side wall while the horizontal direction is along the side wall parallel to the axis of the hole. The solidification model derived in [7] is stated below.

We consider an incompressible fluid contained in the vertical direction by a bottom defined by $y = \psi(x,t)$ and a top defined by $y = \psi(x,t) + H(x,t)$ as indicated in Figure 3, where x and y are the coordinates in the horizontal (along the side wall) and vertical (perpendicular to the side wall) directions and t is time. Solidified material is present in the region $y < \psi(x,t)$. The horizontal velocity is denoted by $u(x,t)$ and the temperature by $\theta(x,y,t)$. We transform to dimensionless variables via $u = U\hat{u}$, $\theta = T_m + (T_v - T_m)\hat{\theta}$, $\psi = d\hat{\psi}$, $H = d\hat{H}$, $x = L\hat{x}$, $y = d\hat{y}$ and $t = L\hat{t}/U$, where T_v is the vaporization temperature at one atmosphere pressure. Henceforth, the hats on the non-dimensional variables will be omitted without ambiguity. The equations in the fluid are given by

$$\frac{\partial H}{\partial t} + \frac{\partial}{\partial x}(uH) = -\frac{\partial \psi}{\partial t}, \qquad \frac{\partial u}{\partial t} + u\frac{\partial u}{\partial x} = 0, \tag{1}$$

$$\frac{\partial \theta}{\partial t} + u\frac{\partial \theta}{\partial x} + \{(u\psi)_x - u_x y\}\frac{\partial \theta}{\partial y} = D\frac{\partial^2 \theta}{\partial y^2}, \tag{2}$$

at the liquid/gas interface,

$$\frac{\partial \theta}{\partial y}(x, \psi + H, t) = 0, \tag{3}$$

at the solid/liquid interface,

$$\lambda_f \frac{\partial \psi}{\partial t} + D\left[\frac{\partial \theta}{\partial y}\right]_{\psi^-}^{\psi^+} = 0, \qquad \theta(x,\psi,t) = 0, \tag{4}$$

and in the solid,

$$\frac{\partial \theta}{\partial t} = D\frac{\partial^2 \theta}{\partial y^2} \quad \text{for} \quad y < \psi \quad \text{and} \quad \theta \to \bar{T}_a \quad \text{as} \quad y \to -\infty. \tag{5}$$

The initial conditions are

$$u(x,0) = \tilde{u}(x), \qquad \theta(x,y,0) = \tilde{\theta}(x,y), \qquad H(x,0) = \tilde{H}(x), \qquad \psi(x,0) = 0. \tag{6}$$

where we assume $\tilde{\theta}(x,y) = \bar{T}_a$ for $y < 0$, and $\tilde{\theta}(x,0) = 0$ and $\partial\tilde{\theta}/\partial y(x, \tilde{H}(x)) = 0$ for $\tilde{H}(x) > 0$. The dimensionless constants D, λ_f and $\bar{T}_a$ are defined, and typical values given in Table 2. The equation for conservation of momentum in [7] has been rewritten as inviscid Burgers' equation as it uncouples from the other equations in the system. The system of equations (1)-(5) are not in conservative form, these equations will be integrated until a shock forms and not beyond.

3 Numerical Solution

3.1 Introduction

In this subsection, an algorithm to discretize the system of equations (1)-(5) is described. The equations are updated explicitly on each time-step. Equations (1) are solved using a reconstruction-evolution algorithm. Equations (2), (3) and (5) employ the extension to the enthalpy method described in [7]. The post processing to obtain the solid/liquid interface uses the Stefan condition (cf. [9]). These are discussed below.

3.2 Reconstruction-evolution algorithm

Inviscid Burgers' equation is discretized as

$$u_i^{n+1} = u_i^n - \frac{\Delta t}{\Delta x}\left(F_{i+1/2}^n - F_{i-1/2}^n\right),$$

where u_i^n is the approximation to $u(i\Delta x,\ n\Delta t)$, Δx is the mesh spacing, Δt is the time-step,

$$F_{i+1/2}^n = \frac{1}{2}(u_i^n)^2 + \frac{a_{i+1/2}^n}{2}\left[1 - a_{i+1/2}^n\frac{\Delta t}{\Delta x}\right]s_i^n\Delta x, \qquad s_i^n = \Phi_{i+1/2}^n(r)\left(\frac{u_{i+1}^n - u_i^n}{\Delta x}\right),$$

$$r = \frac{u_i^n - u_{i-1}^n}{u_{i+1}^n - u_i^n}, \qquad a_{i+1/2}^n = \begin{cases} (u_{i+1}^n + u_i^n)/2 & u_{i+1}^n \neq u_i^n, \\ 0 & u_{i+1}^n = u_i^n, \end{cases}$$

and the superbee flux limiter $\Phi_{i+1/2}^n(r) = \max(\min(1,\ 2r),\ \min(r,\ 2))$. The equation for conservation of mass is discretized as

$$H_i^{n+1} = H_i^n - \frac{\Delta t}{\Delta x}\left(\bar{F}_{i+1/2}^n - \bar{F}_{i-1/2}^n\right) - (\psi_i^n - \psi_i^{n-1}),$$

where H_i^n is the approximation to $H(i\Delta x,\ n\Delta t)$, ψ_i^n is the approximation to $\psi(i\Delta x,\ n\Delta t)$,

$$\bar{F}_{i+1/2}^n = u_i^n H_i^n + \frac{\bar{a}_{i+1/2}^n}{2}\left[1 - \bar{a}_{i+1/2}^n\frac{\Delta t}{\Delta x}\right]\bar{s}_i^n\Delta x, \qquad \bar{s}_i^n = \Phi_{i+1/2}^n(\bar{r})\left(\frac{H_{i+1}^n - H_i^n}{\Delta x}\right),$$

$$\bar{r} = \frac{H_i^n - H_{i-1}^n}{H_{i+1}^n - H_i^n}, \qquad \bar{a}_{i+1/2}^n = \frac{1}{2}(u_{i+1}^n + u_i^n).$$

3.3 Lagrangian-enthalpy method

3.3.1 Enthalpy formulation

We define the dimensionless enthalpy, E, by

$$E = \begin{cases} \theta & \theta < 0 \quad \text{(solid)}, \\ \theta + \lambda_f & \theta > 0 \quad \text{(liquid)}, \end{cases}$$

and therefore

$$\theta = \begin{cases} E & E < 0, \\ 0 & 0 < E < \lambda_f, \\ E - \lambda_f & E > \lambda_f. \end{cases} \tag{7}$$

The classical formulation of (2) and $(5)_1$ may be written in the form

$$\frac{\partial E}{\partial t} + \frac{\partial}{\partial x}(\chi u\theta) + \frac{\partial}{\partial y}\left(\chi\left\{\frac{\partial}{\partial x}(u\psi) - \frac{\partial u}{\partial x}y\right\}\theta - D\frac{\partial\theta}{\partial y}\right) = 0, \tag{8}$$

for (x, y, t) in the solid or liquid, where χ is the Heaviside function

$$\chi = \begin{cases} 0 & \theta < 0 \quad \text{(solid)}, \\ 1 & \theta > 0 \quad \text{(liquid)}. \end{cases}$$

The discretization of (3), $(5)_2$, (7) and (8) is required in this subsection.

3.3.2 Lagrangian step

The solution of the enthalpy formulation is required on a time-dependent domain. Our explicit discretization means that on each time-step the domain of computation is prescribed. We chose to represent the temperature and enthalpy on a rectangular mesh $[0, A^n] \times [-B, C]$, where A, B and C are positive constants and $A^{n-1} \leq A^n < A$. The domain of computation is allowed to expand as the fluid traverses the solid so that unnecessary computations are obviated (see Figure 4).

The question of how to discretize the advection and convection of the fluid in the region between the solid/liquid and liquid/gas interfaces is now addressed. We evaluate the Lagrangian description of motion by solving

$$\frac{\partial \theta}{\partial t} + u\frac{\partial \theta}{\partial x} + \{(u\psi)_x - u_x y\}\frac{\partial \theta}{\partial y} = 0,$$

along the bicharacteristics

$$\frac{\mathrm{d}x}{\mathrm{d}t} = u, \qquad \frac{\mathrm{d}y}{\mathrm{d}t} = (u\psi)_x - u_x y, \qquad \text{with} \qquad \frac{\mathrm{d}\theta}{\mathrm{d}t} = 0.$$

The temperature is constant along the fluid path. The bicharacteristic is integrated backwards in time from the fixed mesh point $(x_i,\ y_j)$ to evaluate the fluid location at the previous time-step $(x_{loc},\ y_{loc})$. The bicharacteristics are discretized as follows

$$x_{loc} = x_i - \Delta t\ u_i^n, \qquad y_{loc} = y_j - \Delta t \left[\phi(\tilde{r})\left(\frac{u_{i+1}^n \psi_{i+1}^n - u_i^n \psi_i^n}{\Delta x}\right) - y_j \left(\frac{u_i^n - u_{i-1}^n}{\Delta x}\right)\right],$$

where $\phi(\tilde{r}) = \max(0,\ \min(1, \tilde{r}))$ is a slope limiter and $\tilde{r} = (u_i^n \psi_i^n - u_{i-1}^n \psi_{i-1}^n)/(u_{i+1}^n \psi_{i+1}^n - u_i^n \psi_i^n)$. The temperature at $(x_{loc},\ y_{loc})$ is evaluated by interpolating (and extrapolating near the interfaces) the values on the previous time-step. This value is used to update the temperature at the fixed mesh point $(x_i,\ y_j)$.

3.3.3 Enthalpy step

The next step is to apply the one-dimensional enthalpy method [2]

$$E_{ij}^{n+1} = E_{ij}^n + \frac{\Delta t\ D}{\Delta y^2}\left(\theta_{ij+1}^n - 2\theta_{ij}^n + \theta_{ij-1}^n\right),$$

along with

$$\theta_{ij}^n = \begin{cases} E_{ij}^n & E_{ij}^n < 0, \\ 0 & 0 < E_{ij}^n < \lambda_f, \\ E_{ij}^n - \lambda_f & E_{ij}^n > \lambda_f. \end{cases}$$

The far-field boundary condition is $\theta_{i0}^n = \bar{T}_a$ at $y = -B$ where $B \gg 1$. The boundary condition at the liquid/gas interface is specified by utilizing the ghost cells above the free surface.

3.4 Solid/liquid interface

A cell $[x_{i-1/2},\ x_{i+1/2}) \times [y_{j-1/2},\ y_{j+1/2})$ is undergoing transition from solid to liquid if $0 < E_{ij}^{n+1} < \lambda_f$. The solid/liquid interface in a cell undergoing transition is updated using

$$\psi_i^{n+1} = \psi_i^n + \frac{D\Delta t}{2\lambda_f}\left[\frac{\theta_{ij}^{n+1} - \theta_{ij-1}^{n+1}}{\Delta y} + \frac{\theta_{ij}^n - \theta_{ij-1}^n}{\Delta y} - \frac{\theta_{ij+1}^{n+1} - \theta_{ij}^{n+1}}{\Delta y} - \frac{\theta_{ij+1}^n - \theta_{ij}^n}{\Delta y}\right] + \frac{f\Delta t}{\Delta x^2}(\psi_{i+1}^n - 2\psi_i^n + \psi_{i-1}^n),$$

where the second term on the right-hand side follows from the Stefan condition $(4)_1$ and the third term smoothes the interface. The smoothing coefficient f is sufficiently small that it only operates on interfaces which are jagged on the length-scale Δx.

This algorithm to determine the solid/liquid interface was developed on a one-dimensional problem where an exact solution was available for comparison.

3.5 Code validation

A number of analytical solutions were employed to validate the code. For example, a generalization of the Neumann solution (see [8, p. 158]) was used to replace the enthalpy method in the code. The propagation of a molten blob of aluminium at melting point is then simulated using both codes. The results are compared to check the accuracy of the enthalpy method against an exact solution.

4 Results

4.1 Introduction

We consider idealizations of stage (iii) of the laser drilling process (see Figure 1). The problem is initiated with a blob of molten aluminium on a solid aluminium surface. The molten aluminium is initially given a linear vertical temperature profile, whereas the solid aluminium has a constant temperature of $T_a = 600$K. We simulate the propagation, melting and solidification for three initial conditions. We chose a uniform mesh across the entire domain. Numerical results have been obtained for a variety of mesh spacings and time-steps to ensure grid independence.

4.2 Larger blob with constant initial velocity

The first simulation corresponds to the larger blob of molten aluminium having a constant initial velocity. The fluid will not develop a shock with this initial condition. Figures 5 and 6 show five snapshots.

During the first 3×10^{-5}s, the molten aluminium has cooled significantly and some of the original solid has melted back. Figure 7 shows the time history of the solid/liquid interface at $x = 8 \times 10^{-4}$m, that is under the initial fluid blob. The molten aluminium initially freezes due to rapid thermal conduction into the cold solid. This chill melts back and melting of the original solid follows due to conduction from the hot fluid. The melting is curtailed by the approach of the trailing edge of the fluid. The molten aluminium then begins to resolidify which terminates abruptly with the passing of the trailing edge of the liquid/gas interface. The edge effects in the temperature contours of the fluid blob (shown in Figure 5) are responsible for the change in the motion of the solid/liquid interface.

The fluid blob at 3×10^{-5}s has narrowed in width but increased in depth. Some of the sensible heat in the molten metal has been converted into latent heat to increase the depth. In Figures 5 and 6, the fluid blob continues to narrow, but the change in depth is less rapid. Steep leading and trailing edges of the blob are clearly visible. (It should be emphasised that Figures 5 and 6 are not drawn on the same horizontal and vertical scales.) The edge effects seen in the temperature contours are responsible for the narrowing.

The molten aluminium cools to its melting temperature as the simulation progresses which has two effects: melting no longer takes place and solidification is more rapid. A larger percentage of the molten aluminium solidifies the further that the blob progresses across the solid aluminium surface. Analysis of the solid/liquid interface in Figure 6 shows that it asymptotes to a growth proportional to $\sqrt{x}$. The entire fluid blob will eventually solidify. This simulation corresponds to a successful attempt to drill a hole of 4mm.

4.3 Smaller blob with constant initial velocity

This second simulation considers a smaller blob of molten aluminium but with a larger temperature gradient. The initial condition for velocity is unchanged. This choice corresponds to laser drilling at higher intensity, except that a smaller drop would be accelerated to a greater speed by the splash.

During the first 3×10^{-5}s, the behaviour is similar to Figure 5 with a chill formation which melts back and then resolidification. The fluid blob narrows in width and increases in depth. After 3×10^{-5}s, the molten aluminium has cooled to a greater extent than in the simulation of a larger blob. Significant solidification has taken place in comparison to Figure 5.

After 6×10^{-5}s, the molten aluminium has cooled to its melting temperature and almost completely solidified. This represents an unsuccessful attempt to drill a hole of 4mm.

4.4 Larger blob with decreasing initial velocity

The third simulation is identical to the first apart from the initial condition for velocity. The initial velocity has a (constant) negative gradient, and, as a result, the fluid will develop a shock after 10^{-4}s. The velocity after the splash is controlled by the radial laser intensity profile.

We compare the results in Figures 5 and 9. The effect of the change of initial velocity is a further narrowing in width and increase in depth. The molten aluminium in Figure 9 has cooled to a lesser extent after 3×10^{-5}s. This simulation corresponds to the least solidified aluminium after 6×10^{-5}s.

The increase in depth continues until the aspect ratio is no longer small. This represents a possible mechanism for the clumps of recast observed in Figure 2. Unfortunately, the simulation is terminated after 8×10^{-5}s; the simplified model (1)-(5) becomes invalid when the aspect ratio of the molten aluminium reaches order one. This simulation corresponds to a successful attempt to drill a hole of 4mm. The side wall of the drilled hole remains mostly free of recast; this is a high quality result.

5 Conclusions

We conclude by offering physical explanations for some of the drawbacks associated with the laser percussion drilling process.
(i) *recast*. In the absence of shocks, the resolidification along the wall of the drilled hole will be in the form of thin layers. The thickness of this layer increases with increasing hole depth. As a result, a smaller proportion of the molten metal escapes the deeper that the hole is drilled. This reflects the observation that the speed of drilling reduces with depth. Moreover, the penetration depth is limited as a result of the molten metal from the base of the hole entirely solidifying against the wall of the hole.
A negative gradient in the initial condition for velocity will result in a shock developing after a finite time. The clumping process prior to shock formation minimizes the solidification of the molten aluminium. However, this process appears to be associated with the large clumps of recast observed.
(ii) *bellow shape*. A local increase in hole diameter has been shown to result from melting of the originally solid wall of the hole by rapid thermal conduction from the hot liquid.
(iii) *tapering* Tapering is not present in our simulations. This is to be expected as it is known to be associated with the focal length of the laser.
The optimal initial velocity is clearly a gentle negative gradient. This must be achieved by accurate control of the radial laser intensity profile during the splash. Freezing of the fluid to the side wall of the drilled hole would decrease in this case and, as a result, the speed of drilling would increase.

References

[1] M. Allmen and A. Blatter, *Laser-Beam Interactions with Materials*, Springer-Verlag, Berlin, 1995.

[2] C. M. Elliott and J. R. Ockendon, *Weak and Variational Methods for Moving Boundary Problems*, Pitman Books Limited, London, 1982.

[3] R. K. Ganesh and A. Faghri, *A generalized thermal modeling for laser drilling process–I. mathematical modeling and numerical methodology*, Int. J. Heat Mass Transfer, 40 (1997), pp. 3351–3360.

[4] ——, *A generalized thermal modeling for laser drilling process–II. numerical simulation and results*, Int. J. Heat Mass Transfer, 40 (1997), pp. 3361–3373.

[5] J. R. Ockendon, S. D. Howison, A. A. Lacey, and A. B. Movchan, *Applied Partial Differential Equations*, Oxford University Press, New York, 1999.

[6] K. Ražnjević, *Handbook of Thermodynamic Tables and Charts*, Hemisphere, London, 1976.

[7] W. R. Smith, *Models for solidification and splashing in laser percussion drilling*, SIAM J. Appl. Math., 62 (2002), pp. 1899–1923.

[8] A. B. Tayler, *Mathematical Models in Applied Mechanics*, Oxford University Press, Oxford, 1986.

[9] V. Voller and M. Cross, *An explicit method to track a moving phase change front*, Int. J. Heat Mass Transfer, 26 (1983), pp. 147–150.

Symbol	Definition	Value
ρ	density	2.7×10^3 kg m $^{-3}$
L_f	latent heat of fusion	3.6×10^5J kg^{-1}
k	thermal conductivity	2.3×10^2 W m^{-1}K^{-1}
c	specific heat capacity	9.0×10^2 J kg^{-1}K^{-1}
T_m	melting temperature	9.3×10^2K
T_v	vaporization temperature	2.5×10^3 K
μ	viscosity	2.7×10^{-3} Pa s
σ	surface tension	1 kg s^{-2}

Table 1: Physical data for drilling aluminium

Symbol	Definition	Typical Value
δ	d/L	0.1
D	$k/\rho cUL\delta^2$	0.2
λ_f	$L_f/c(T_v - T_m)$	0.3
$\bar{T}_a$	$(T_a - T_m)/(T_v - T_m)$	-0.2

Table 2: Dimensionless parameters for a typical laser percussion drilling process

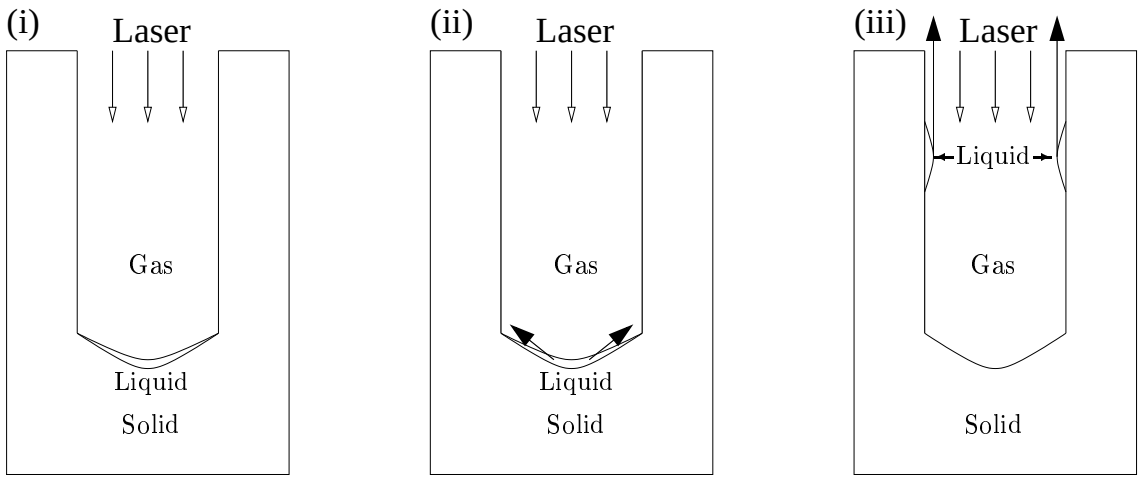

Figure 1: A schematic of the three stages in laser percussion drilling (i) melt-pool formation at the base of the drilled hole, (ii) splashing of the melt pool away from the axis of the drilled hole and (iii) solidification of the molten metal as it moves along the side wall. The filled arrows represent fluid motion and the unfilled arrows laser energy.

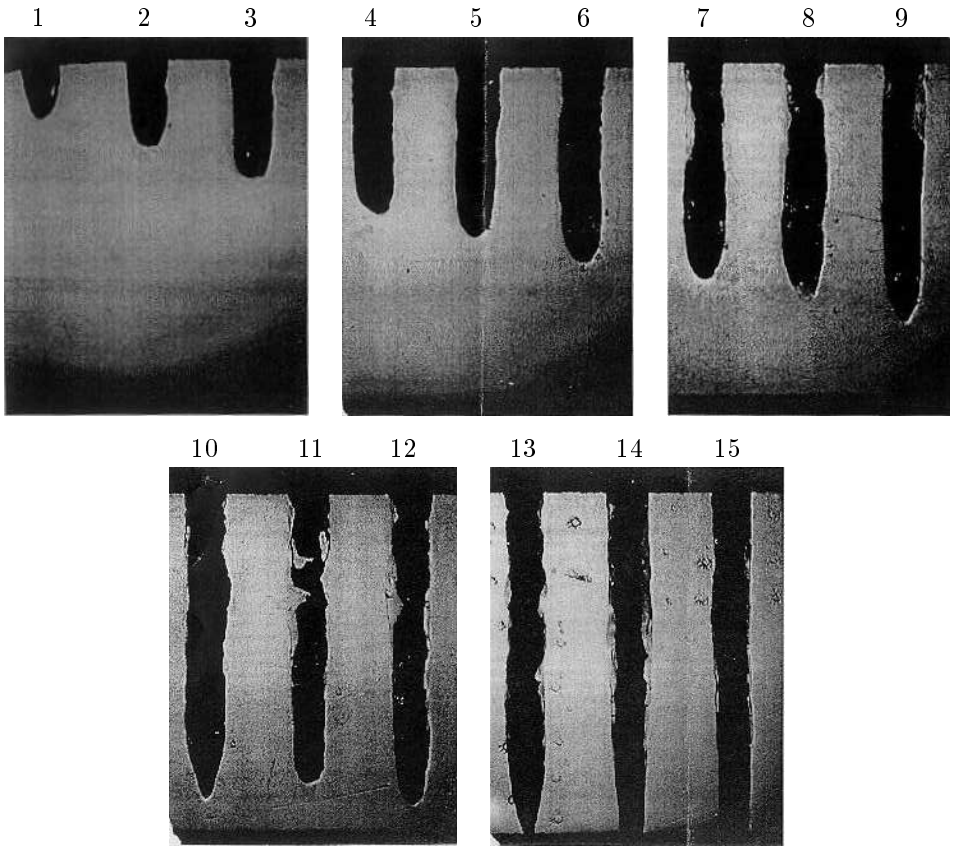

Figure 2: A series of photographs of holes produced by laser percussion drilling. The number of pulses to produce each hole is indicated (Courtesy of Eldim BV).

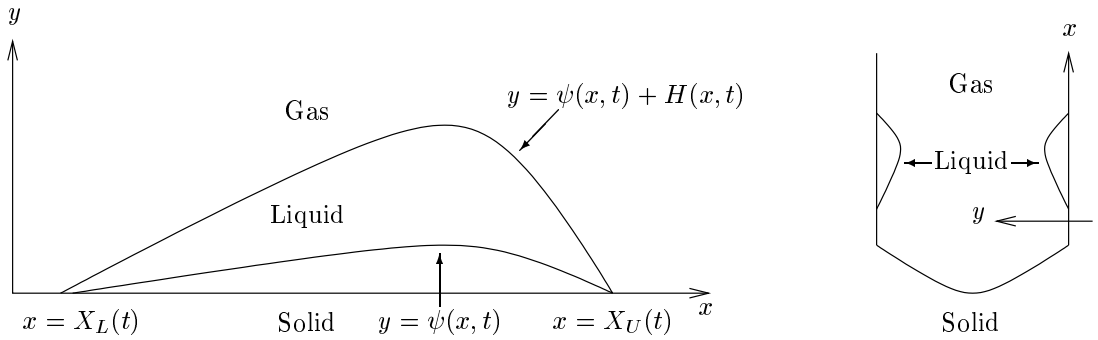

Figure 3: On the left the planar representation of solidification and on the right its interpretation on a drilled hole. The horizontal direction is denoted by x and the vertical direction by y. The incompressible fluid is in the region $X_L(t) < x < X_U(t)$ and $\psi(x,t) < y < \psi(x,t) + H(x,t)$, and the solid is in the region $y < \psi(x,t)$.

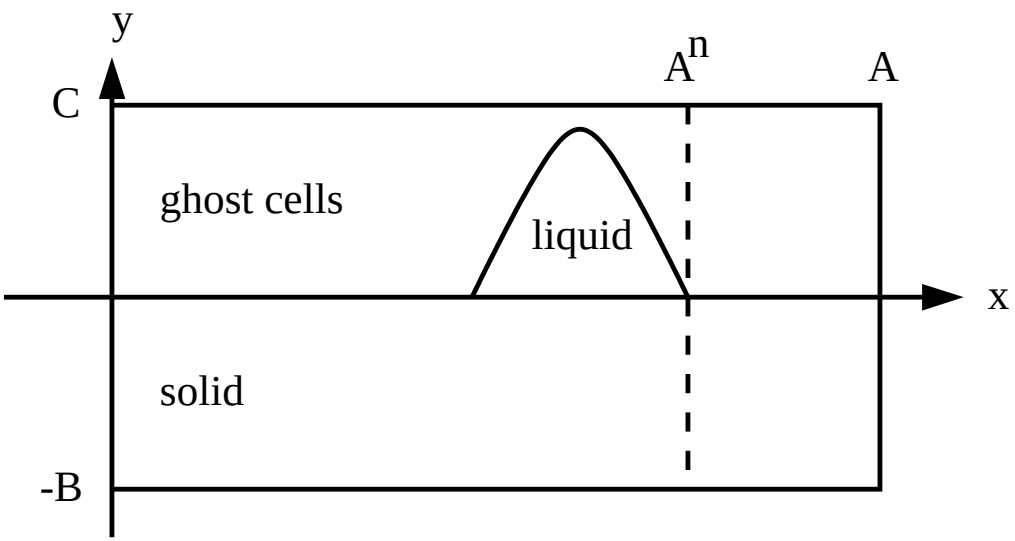

Figure 4: A schematic of the domain of computation at time t^n. The domain of computation is to the left of the dashed line.

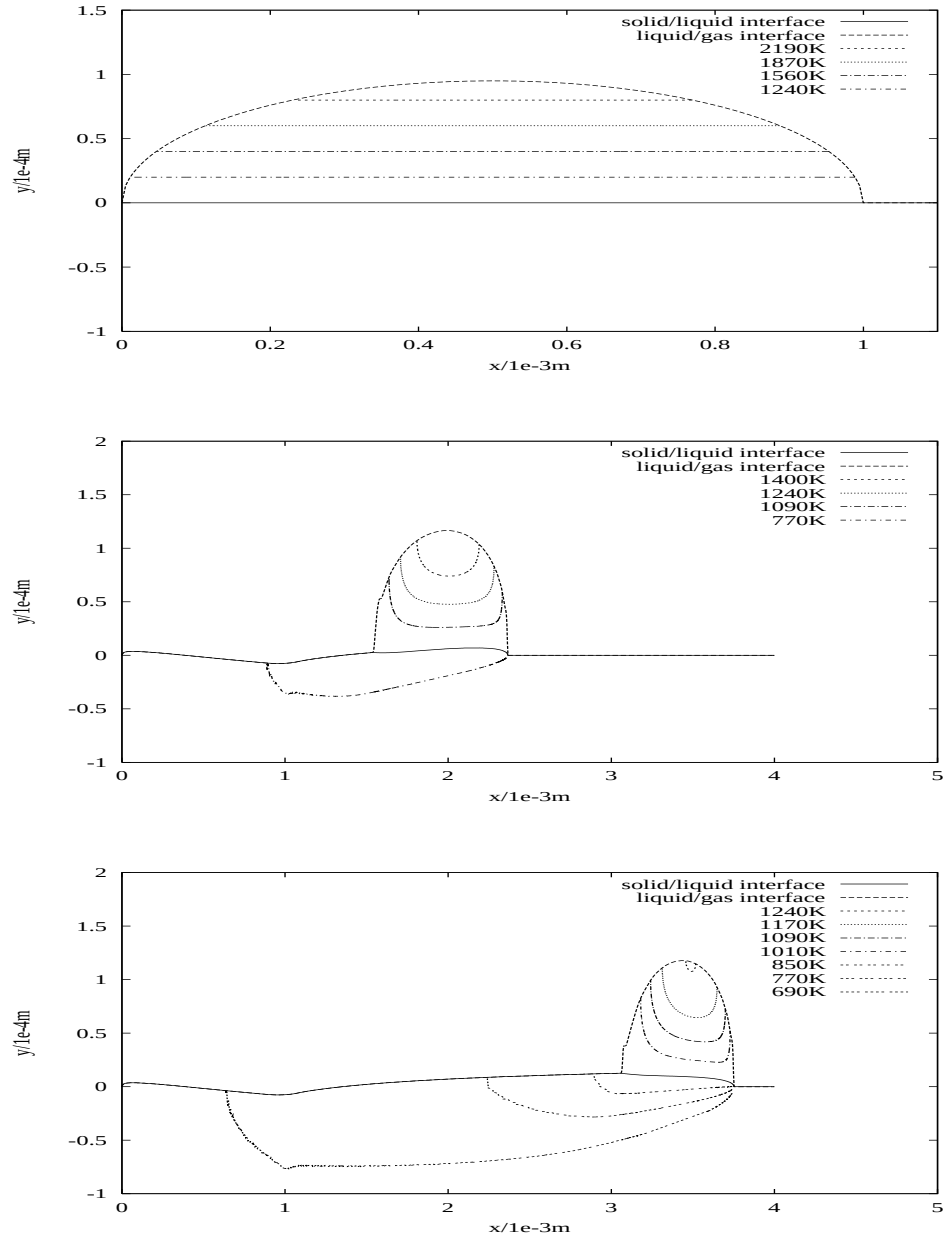

Figure 5: Propagation and solidification of a molten drop of aluminium with the data in Table 1, dimensional $u(x,0) = 50\text{ms}^{-1}$ and $T_a = 600\text{K}$ at times $t = 0$ (top), $t = 3 \times 10^{-5}\text{s}$ (middle) and $t = 6 \times 10^{-5}\text{s}$ (bottom). Temperature contours are shown alongside the solid/liquid and liquid/gas interfaces.

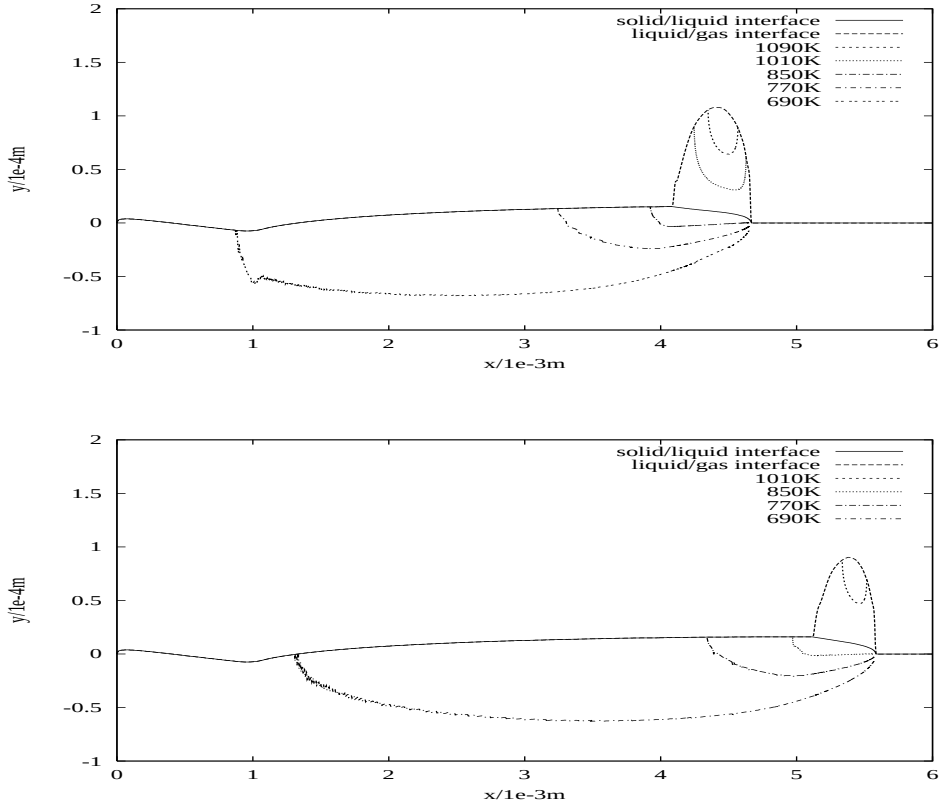

Figure 6: Propagation and solidification of a molten drop of aluminium with the data in Table 1, dimensional $u(x,0) = 50\text{ms}^{-1}$ and $T_a = 600\text{K}$ at times $t = 8 \times 10^{-5}\text{s}$ (top) and $t = 1 \times 10^{-4}\text{s}$ (bottom). Temperature contours are shown alongside the solid/liquid and liquid/gas interfaces.

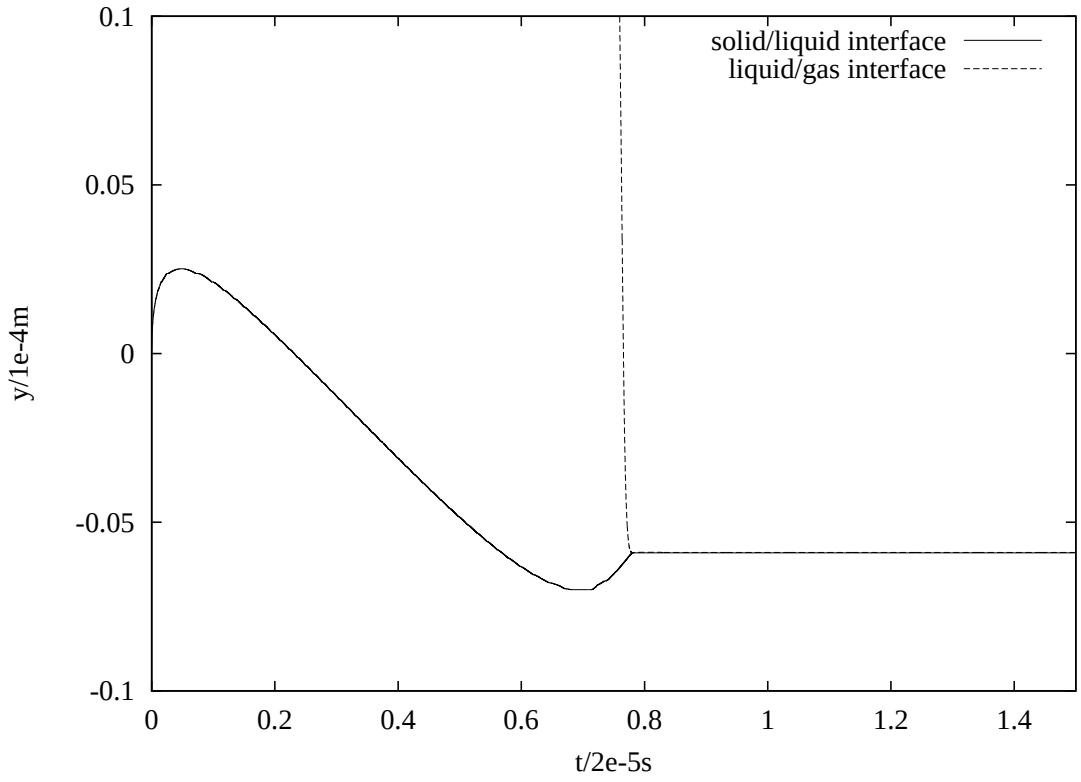

Figure 7: History of the location $x = 8 \times 10^{-4}$m for the problem described in Figure 5.

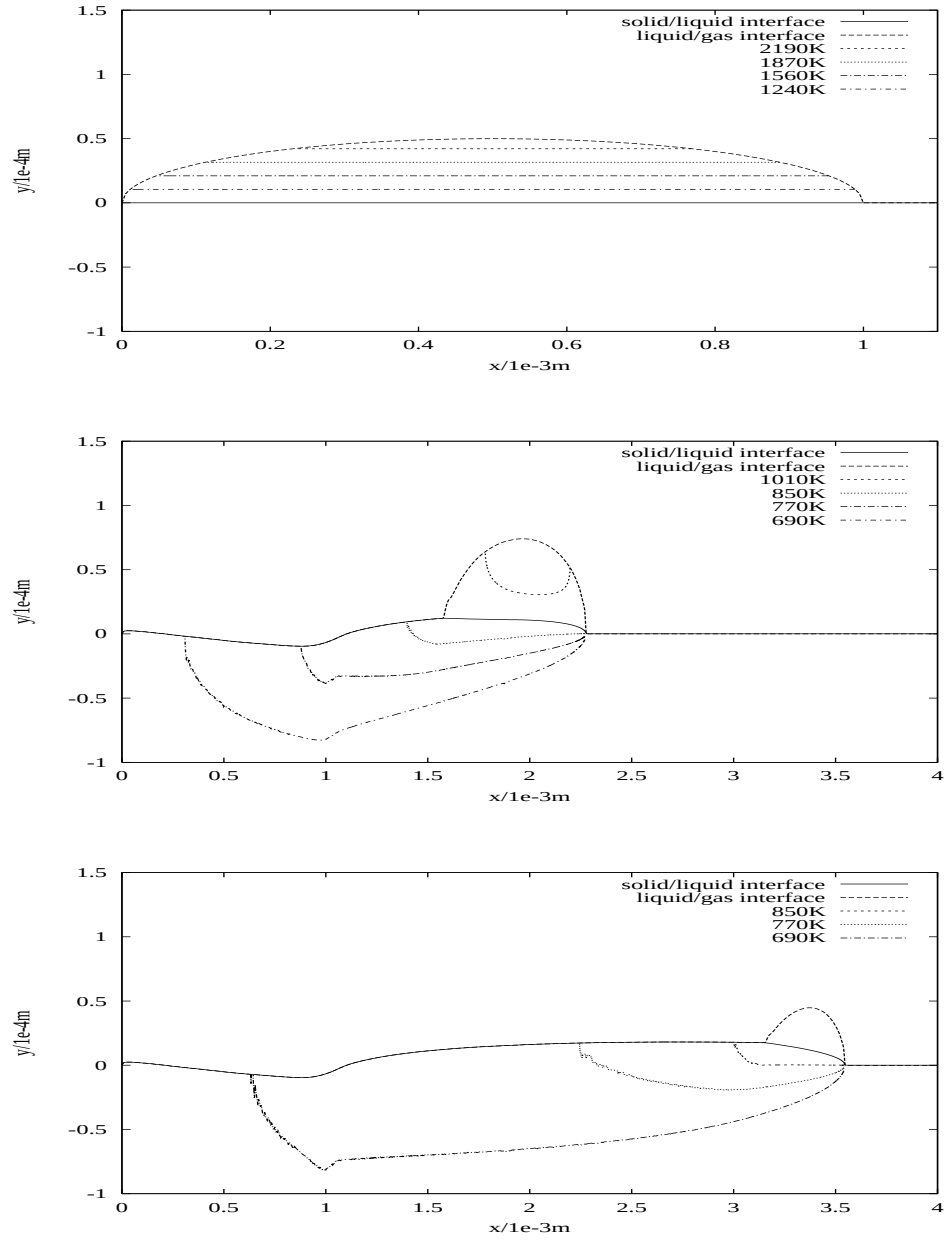

Figure 8: Propagation and solidification of a molten drop of aluminium with the data in Table 1, dimensional $u(x,0) = 50\text{ms}^{-1}$ and $T_a = 600\text{K}$ at times $t = 0$ (top), $t = 3 \times 10^{-5}\text{s}$ (middle) and $t = 6 \times 10^{-5}\text{s}$ (bottom). Temperature contours are shown alongside the solid/liquid and liquid/gas interfaces.

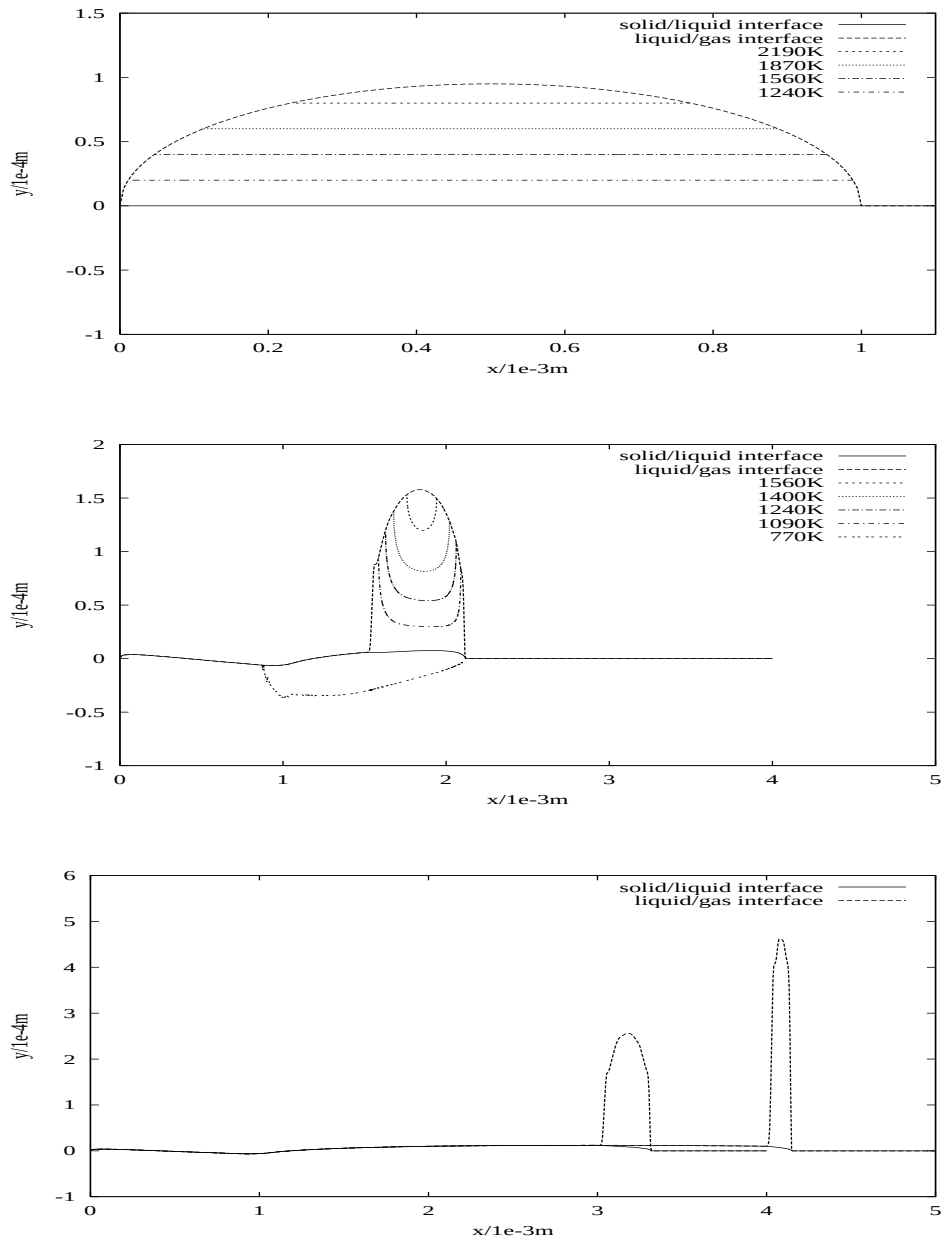

Figure 9: Propagation and solidification of a molten drop of aluminium with the data in Table 1 and T_a = 600K at times $t = 0$ (top), $t = 3 \times 10^{-5}$s (middle), $t = 6 \times 10^{-5}$s (bottom) and $t = 8 \times 10^{-5}$s (bottom). The dimensional $u(x, 0) = 40\text{ms}^{-1} + (1 - x/1mm) \times 10\text{ms}^{-1}$. Temperature contours are shown alongside the solid/liquid and liquid/gas interfaces at $t = 0$ and $t = 3 \times 10^{-5}$s.